

# D2SA: Dual-Stage Distribution and Slice Adaptation for Efficient Test-Time Adaptation in MRI Reconstruction

Lipei Zhang<sup>1</sup>, Rui Sun<sup>2</sup>, Zhongying Deng<sup>1</sup>, Yanqi Cheng<sup>1</sup>,  
Carola-Bibiane Schönlieb<sup>1</sup>, Angelica I Aviles-Rivero<sup>3</sup>

<sup>1</sup> Department of Applied Mathematics and Theoretical Physics, University of Cambridge

<sup>2</sup> School of Science and Engineering (SSE), The Chinese University of HongKong, ShenZhen

<sup>3</sup> Yau Mathematical Sciences Center, Tsinghua University

## Abstract

Variations in Magnetic resonance imaging (MRI) scanners and acquisition protocols cause distribution shifts that degrade reconstruction performance on unseen data. Test-time adaptation (TTA) offers a promising solution to address these discrepancies. However, previous single-shot TTA approaches are inefficient due to repeated training and suboptimal distributional models. Self-supervised learning methods are also limited by scarce data scenarios. To address these challenges, we propose a novel Dual-Stage Distribution and Slice Adaptation (D2SA) via MRI implicit neural representation (MR-INR) to improve MRI reconstruction performance and efficiency, which features two stages. In the first stage, an MR-INR branch performs patient-wise distribution adaptation by learning shared representations across slices and modelling patient-specific shifts with mean and variance adjustments. In the second stage, single-slice adaptation refines the output from frozen convolutional layers with a learnable anisotropic diffusion module, preventing over-smoothing and reducing computation. Experiments across four MRI distribution shifts demonstrate that our method can integrate well with various self-supervised learning (SSL) framework, improving performance and accelerating convergence under diverse conditions.

## 1. Introduction

Magnetic resonance imaging (MRI) captures detailed tissue structures using k-space sampling. In clinical practice, MRI is often under-sampled to accelerate scan time and reduce patient burden. However, under-sampling results in an ill-posed inverse problem, making accurate MRI reconstruction challenging [23]. Traditional compressed sensing techniques attempt to address this through iterative reconstruction algorithms [3–5, 28], but these methods are computationally

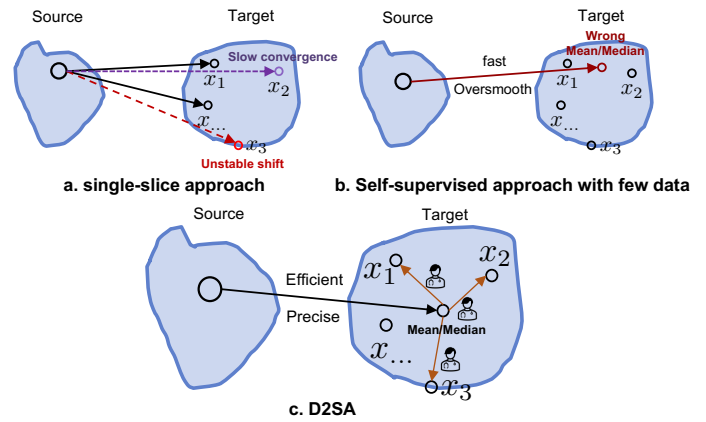


Figure 1. Illustration of TTA strategies for MRI reconstruction under distribution shifts. (a) Single-slice methods can be slow and unstable. (b) Self-supervised approaches risk over-smoothing or wrong mean/median with limited data. (c) D2SA adapts efficiently and precisely to unknown distributions at the patient level, and supports single-slice refinements on demand of doctor.

tionally expensive and less accurate. Recent advances in deep learning have significantly improved both reconstruction speed and quality by learning direct mappings from raw data [18], such as unrolled networks [27], plug-and-play frameworks [1], and diffusion models [8].

Despite these advancements, deep learning models struggle with adapting to diverse clinical scenarios due to two primary challenges. Firstly, limited MRI data for model adaptation: MRI datasets are difficult to collect, making it challenging to generalise deep models without overfitting. Secondly, distribution shifts between training and test data: In real-world deployment, MRI scans may be acquired under different conditions (e.g., scanner types, patient demographics), causing performance degradation due to mismatched data distributions between training and test sets [10, 11]. An ideal MRI reconstruction model should therefore balance three key goals for overcoming distri-

bution shifts: 1) *Strong adaptation to new distributions* – maintaining high performance despite distribution shifts. 2) *Robustness to limited data* – preventing overfitting in data-scarce scenarios. 3) *Fast convergence* – minimising adaptation time at test time.

Most existing methods focus primarily on distribution generalisation but fail to optimise all three goals simultaneously. Test-time adaptation (TTA) techniques partially address this, i.e., they mitigate the distribution shift by updating models on the fly using only test data. Besides handling distribution shifts, batch-based TTA methods (e.g., Noiser2noise [12], FINE [37], SSDU [35]) further enforce self-supervised learning across multiple slices to facilitate fast convergence. However, this batch-wise approach may overfit shared features across slices while ignoring slice-specific variations, leading to over-smoothed reconstructions. Conversely, single-slice-based TTA methods [34, 40] improve fine-grained adaptation but require repeated optimisation cycles, significantly increasing computational overhead. More recent diffusion-based models [2, 9] generate realistic slices for adaptation but are computationally expensive and prone to overfitting on smaller datasets.

To effectively balance all three goals, we propose Dual-Stage Distribution and Slice Adaptation (D2SA). D2SA leverages both patient-wise and slice-wise adaptation through a two-stage process. The first stage models single patient distribution using a small number of slices as prior knowledge. The second stage utilises this learned prior for fast adaptation to each slice, and further introduces an anisotropic diffusion (AD) module to enhance denoising [7, 21] while preventing over-smoothing the structural details. It thus achieves fast adaptation with high reconstruction quality. Both stages treat each MRI slice as a continuous function rather than a static matrix, drawing inspiration from Functa [14] and implicit neural representations (INR)[25]. This function-based perspective allows us to interpret distribution shifts as small function-level variations, e.g., functions with different mean/variance variables in the feature space. Owing to the adaptive mean/variance, this function-centric approach can be efficiently adapted to new distributions without the need for extensive data for retraining. It also enables the plug-in of networks at test time, thus highly flexible. Our novel approach ensures fast convergence, robustness to limited data, and strong generalisation to new distributions, addressing a critical gap in MRI reconstruction research. To sum up, our contributions are

- **Functional-Level Patient Adaptation.** We develop an INR-based strategy that learns a patient’s distribution from a small number of slices, with the INR trained to capture individualised mean and variance shifts for the second-stage fast adaptation.
- **Structural-Preserving Single-Slice Refinement.** After

modelling patient-level shifts, the pre-trained INR rapidly refines each slice. We introduce a learnable Anisotropic Diffusion (AD) module to maintain structural fidelity, reduce over-smoothing, and limit computation by freezing the main convolutional layers.

- **Extensive Validation.** We evaluate D2SA on four distribution shift scenarios, using both UNet [26] and a variational network [31]. Results demonstrate robust and efficient reconstruction across diverse clinical conditions.

## 2. Related Works

**TTA for Medical Imaging.** Test-time adaptation (TTA) addresses distribution shifts in medical imaging by leveraging unlabelled test data to refine models pre-trained on source domains [22]. The core challenge is constructing supervision signals when test labels are unavailable, often achieved through consistency regularisation or self-supervised loss. Consistency Regularisation enforces stable predictions under perturbed inputs. PINER [30] uses implicit neural representation (INR) learning to represent CT slices at different resolutions, selecting the closest match to reduce shifts. Steerable diffusion models [2] enforce consistency for realistic reconstructions. Self-Supervised Learning designs pretext tasks, such as contrastive learning [19] or rotation prediction [17]. DIP-TTT [11] applies self-supervision to reconstruct under-sampled single image under multiple shifts. Meta-TTT [34] extends this by incorporating meta-learning to reduce overfitting on limited test data. Unlike computationally expensive slice-wise TTA methods, we propose a dual-stage TTA framework that first adapts at the patient level to enhance the efficiency and effectiveness of single-slice adaptation.

**INRs for Functional-level Learning.** Implicit neural representations (INRs) model continuous data efficiently, enabling batch training in deep learning workflows. Functa [13] encodes entire datasets as INRs, allowing direct operation on continuous functions rather than discrete arrays. DeepSDF [25] learns continuous signed distance functions (SDFs) for 3D shape modelling, parameterising each shape with a latent code and autoencoder for query-based reconstruction. In biomedical imaging, INRs effectively capture anatomical structures, such as complex airway trees [39], facilitating batch optimisation. Various INR approaches exist, each with unique advantages [15], but SIREN [29] remains the preferred choice for representing high-frequency biomedical data due to its sine-activated architecture, making it well-suited for our adaptation framework.

## 3. Problem Setup

First, MRI reconstruction is an inverse problem where the goal is to recover  $x^* \in \mathbb{C}^N$  from undersampled measure-

ments  $y \in \mathbb{C}^M$  with  $M \ll N$ :

$$y = Ax^* + \epsilon, \quad (1)$$

where  $A$  is the measurement operator, and  $\epsilon$  represents noise. In multi-coil MRI, the acquired measurements for each coil  $i$  follow:

$$y_i = MFS_i x^* + \epsilon, \quad i = 1, \dots, n_c, \quad (2)$$

where  $S_i$  denotes the coil sensitivity map,  $F$  is the 2D Fourier transform.  $M$  is the undersampling mask which can be the 1D cartesian mask, or others [36]. The individual coil images  $x_i = F^{-1}y_i$  are then combined via root-sum-of-squares to reconstruct  $x$ .

Reconstruction is framed as an optimisation problem:

$$\hat{x} = \arg \min_x \frac{1}{2} \|Ax - y\|_2^2 + \lambda R(x), \quad (3)$$

where  $R(x)$  encodes prior knowledge (e.g., wavelet  $\ell_1$ , total variation, or CNN-based priors), and  $\lambda$  controls the balance between data fidelity and regularisation. However, standard reconstruction models assume a fixed distribution during training, limiting their ability to generalise to new datasets or acquisition conditions.

Domain shifts from scanners, anatomy, or acquisition protocols degrade performance. Existing TTA methods can address this but they rely on repeated single-slice training [11] or self-supervised learning on large datasets [12, 35, 37], lacking stability in data-scarce scenarios. To address this, we introduce a D2SA that first learns patient-wise distributions explicitly for better initialisation, enabling more stable and efficient refinement in the second stage.

## 4. Method

To address data scarcity and domain shifts, we propose D2SA, a patient-wise TTA framework that eliminates the need for large datasets and repeated single-slice training. It adapts in two stages, as shown in Figure 2: (1) Patient-Wise Distribution Adaptation, where MR-INR learns shared representations across slices of patients and adjusts variance shifts  $\alpha$  and nonzero-mean shifts  $\beta$ ; (2) Single-Slice Adaptation, which refines single slice efficiently with a learnable anisotropic diffusion (AD) module and frozen original convolutional layers, leveraging improved model initialisation. Next, we introduce the details of each step.

### 4.1. Functional-Level Patient Adaptation

In Figure 2, the MR-INR branch models the structure and distribution of patient-wise data. Inspired by FunctA [14] and DeepSDF [25], which use implicit neural representations (INRs) to encode data as continuous functions, our approach shifts from learning on discrete datasets to learning in function spaces. This enables efficient adaptation to

new unknown distributions, better handling of few-shot scenarios, and improved patient-wise learning capabilities.

In Figure 2.a, each slice in this patient set can we assume the prior distribution over a 1D latent code  $z_i$  as zero-mean multivariate-Gaussian with a spherical covariance  $\sigma^2 I$ . In this work,  $\sigma$  is set to 0.01. The random Fourier coordinates will be calculated by geometric coordinates  $\phi$  of each slice. The input  $\tilde{\gamma}$  for MR-INR is from concatenation of  $z_i$  and  $\phi$ .

$$\tilde{\gamma}(\phi, z_i) = [z_i, \cos(2\pi B\phi), \sin(2\pi B\phi)], \quad (4)$$

where the transformation matrix  $B$  is sampled from a Gaussian distribution  $\mathcal{N}(0, \omega^2)$ .

After this step, we use the standard batch training protocol, where all slices of the current patient are trained per epoch. In the MR-INR branch, the corresponding latent code and Fourier coordinates are modulated and passed through a SIREN [29] network  $f_\theta$  architecture. The ability of Siren and Fourier feature [32] to efficiently model target representation and stability has been shown in [15]. This MR-INR branch can be formed as:

$$\begin{aligned} [\hat{x}, \alpha, \beta] &= f_\theta(\tilde{\gamma}(\phi^i, z)) \\ &= W_n(\Gamma_{n-1} \circ \Gamma_{n-2} \circ \dots \circ \Gamma_0)(\tilde{\gamma}(\phi^i, z)) + b_n, \\ h^{(i+1)} &= \Gamma_i(h^{(i)}) = \sin(W_i h^{(i)} + b_i), \end{aligned} \quad (5)$$

Here,  $\Gamma_i : \mathbb{R}^{M_i} \rightarrow \mathbb{R}^{N_i}$  represents the  $i^{th}$  transformation layer. Each layer applies an affine transformation with weight matrix  $W_i \in \mathbb{R}^{N_i \times M_i}$  and bias  $b_i \in \mathbb{R}^{N_i}$ , followed by a sine activation function. The final layer produces  $[\hat{x}, \alpha, \beta]$  through three output heads.  $\hat{x}$  with dimension  $(B, 1, H, W)$ , represents the predicted pixel intensity for MRI reconstruction.  $\alpha$  variance shifts and  $\beta$  nonzero-mean shifts, with dimension  $(B, C, H, W)$ , modulate feature maps before the final layer via an affine transformation, as shown in Figure 3.a, where  $C$  is the number of feature channels. This formulation enables a shared base network to model common structures while adapting to patient-specific variations, ensuring a compact and efficient solution for test-time adaptation.

Meanwhile, in the first stage, under-sampled MR images from the target domain are input into the network  $g_\delta$ , initialised with source domain pre-trained weights, for TTA ( $g_\delta \rightarrow g_{\delta+\Delta}$ ). Unlike standard adaptation, feature maps before last layer are extracted and adjusted via the affine transformation using  $\alpha$  and  $\beta$ , as illustrated in Figure 3.a.

The predicted MR image from this branch is used to compute the self-supervised loss  $\mathcal{L}_{\text{self}}$  such as Noiser2noise [12, 24], SSDU [35] and fidelity-based FINE [37]. The  $\mathcal{L}_{\text{self}}$  combines with other two loss from MR-INR for joint optimisation. For MR-INR, we adopt a joint optimisation strategy similar to the auto-decoder framework [25], optimising both latent codes and network parameters. The optimisation for the first stage is formulated as:

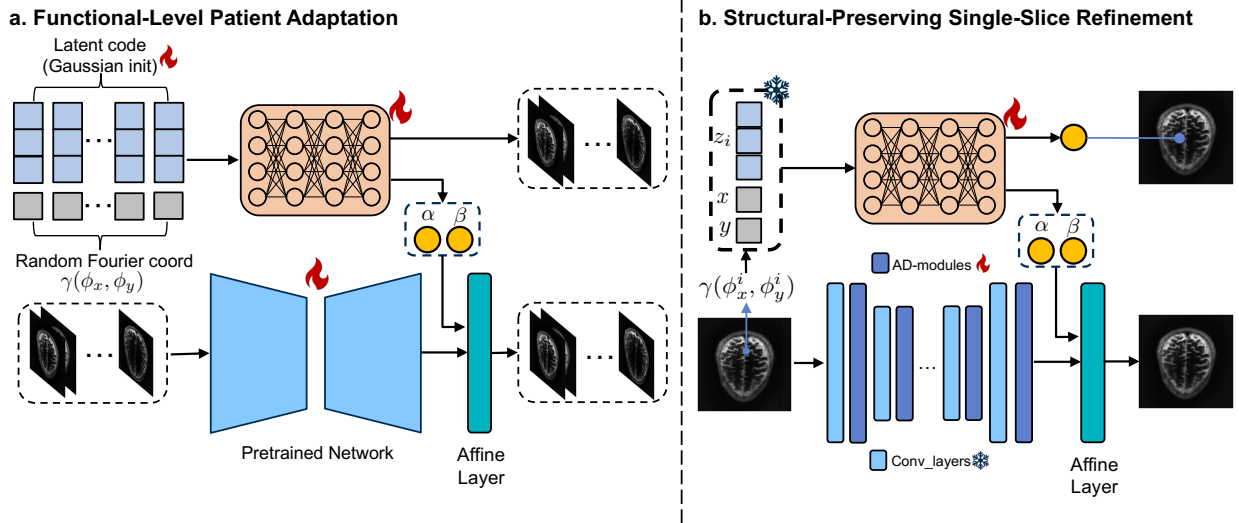


Figure 2. Overview of the proposed two-stage D2SA framework. (a) Functional-Level Patient Adaptation: An INR with a Gaussian-initialized latent code and random Fourier coordinates captures patient-level mean/variance shifts. The “fire” icon indicates trainable modules, including the “pretrained” network and the affine layer. (b) Structural-Preserving Single-Slice Refinement: Here, the main convolutional layers and learned latent code (marked by the “snow” icon) are frozen, while a learnable Anisotropic Diffusion (AD) module and the INR refine individual slices, preserving structural details and finalising outputs via the affine layer.

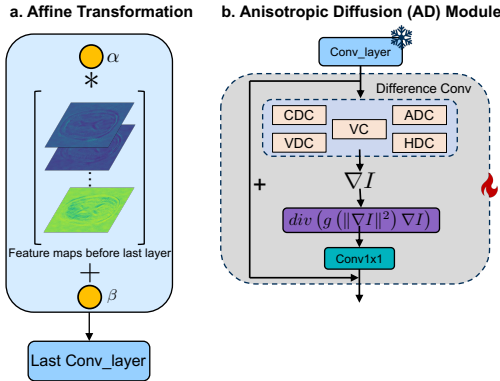


Figure 3. (a) Learnable affine transform scales feature maps by  $\alpha$  and  $\beta$  before the final layer. (b) Learnable anisotropic diffusion (AD) module refines images while preserving structures, with frozen convolution (snowflake) and difference convolution.

$$\hat{\theta}, \hat{z}, \hat{\Delta} = \arg \min_{\theta, z, \Delta} \lambda_{\text{INR}} \sum_{(x_j, z_j, y_j) \in X} \mathcal{L}_1(Af(\tilde{\gamma}(\phi^j, z), \theta), y_j) + \lambda_{\text{reg}} \frac{1}{\sigma^2} \|z\|_2^2 + \lambda_{\text{self}} \sum_{(x_j) \in X} \mathcal{L}_{\text{self}}(g(x_j, \alpha, \beta, \delta + \Delta)). \quad (6)$$

Here,  $\mathcal{L}_1(Af(\tilde{\gamma}(\phi^j, z), \theta), y_j)$  ensures INR predictions aligning with MR signal reconstruction. The regularisation term  $\frac{1}{\sigma^2} \|z\|_2^2$  constrains the latent codes, improving convergence and preventing overfitting. The final term updates weights  $\delta + \Delta$  to adapt to patient-specific variations using self-supervised learning.  $\lambda_{\text{self}}$ ,  $\lambda_{\text{INR}}$  and  $\lambda_{\text{reg}}$  are used for balancing every loss contribution.

## 4.2. Structural-Preserving Single-Slice Refinement

To refine MRI reconstruction at the slice level, we introduce a single-slice adaptation strategy for fine-grained adjustments. Unlike patient-wise adaptation, which learns shared representations across slices, this stage optimises each slice independently to capture localised variations, as shown in Figure 2.b. Here, the latent codes are frozen to preserve the learned global prior information from patient-wise training. This prevents instability and avoids overfitting to slice-specific noise. Instead, the SIREN weights remain trainable, allowing the model to refine its implicit function for each slice. The affine modulation parameters  $\alpha, \beta$  continue adjusting the final feature maps via scaling and shifting.

In the other branch, we adopt a similar DIP-based TTT strategy [11] for single-slice adaptation. This approach leverages CNNs’ strong image priors for structural preservation and optimises a self-supervised loss  $\mathcal{L}_{\text{self}}$  on under-sampled test measurements. To improve efficiency, we freeze all convolutional layers except the final one, reducing unnecessary updates and accelerating optimisation.

A key challenge in batch training is its tendency to learn mean or median representations, leading to over-smoothing that can obscure fine textures and edges. This is critical in MRI, where structural details must be preserved. To address this, we introduce an Anisotropic Diffusion (AD) module, inspired by its shape-preserving properties in image denoising [6, 7]. As shown in Figure 3.b, the AD module refines structural details while suppressing noise by integrating diffusion filtering into the adaptation process.



Given an set of feature  $u$ , the AD equation is:

$$\begin{cases} \left(\frac{\partial u}{\partial t}\right) = \text{div}(g(|\nabla u|)\nabla u) \\ g(|\nabla u|) = \frac{1}{1 + \frac{|\nabla u|^2}{k^2}} \end{cases} \quad (7)$$

When the gradient magnitude is small ( $|\nabla u| \rightarrow 0$ ), the diffusion coefficient  $g$  approaches one, leading to isotropic smoothing similar to Gaussian filtering. Near object boundaries, where  $|\nabla u| \rightarrow 1$ ,  $g$  approaches zero, preventing diffusion and preserving fine details. This allows Anisotropic Diffusion to suppress noise effectively while maintaining sharp edges, making it well-suited for edge-aware regularisation in reconstruction.

We enhance traditional convolutions by integrating difference-based operators [7] that explicitly encode gradient information  $\nabla u$ . Five types of convolutions are introduced: Vanilla Convolution (VC), Central Difference Convolution (CDC), Angular Difference Convolution (ADC), Horizontal Difference Convolution (HDC), and Vertical Difference Convolution (VDC). These capture multiple directional gradients, incorporating concepts from Sobel, Prewitt, and Scharr filters directly into the convolution process [7]. The convolution operation is formulated as:

$$\begin{aligned} \nabla u = F_{\text{out}} &= \text{DConv}(F_{\text{in}}) = \sum_{i=1}^5 F_{\text{in}} * K_i \\ &= F_{\text{in}} * K_{\text{cvt}}, \end{aligned} \quad (8)$$

where  $F_{\text{in}}$  and  $F_{\text{out}}$  represent input and output feature maps, respectively. Instead of separate convolutions, we merge all five kernels  $K_i$  into a single equivalent kernel  $K_{\text{cvt}}$  using a re-parameterisation technique. To improve efficiency, we reduce the number of output feature maps to 1/4 of the original channels, ensuring compact gradient extraction while minimising redundancy.

In calculation of AD equation (7), the computed  $\nabla u$  is used to determine the diffusion coefficient  $g$ , while the divergence  $\text{div}(\cdot)$  is approximated via a 2D Laplacian kernel, which is more efficient to preserve spatial information than standard finite difference methods [38]. The output of the first equation in (7) is restored to its original feature map dimensions using a  $1 \times 1$  convolution. Setting the diffusion step size  $\Delta t = 1$  in (7), the updated feature maps are:

$$u_{i+1} = u_i + \Delta t \cdot \text{div}(g(|\nabla u_i|)\nabla u_i). \quad (9)$$

In this stage, we optimise the weights in MR-INR and the original network with AD module. The final loss function for the second step is:

$$\begin{aligned} \hat{\theta}, \hat{\Delta} &= \arg \min_{\theta, \Delta} \sum_{(x_j, y_j) \in X} \underbrace{\lambda_{\text{INR}} \mathcal{L}_1(Af(\tilde{\gamma}(\phi^j, \hat{z}), \theta), y_j)}_{\text{MR-INR Recon Loss}} \\ &+ \sum_{(y_j) \in X} \underbrace{\lambda_{\text{INR}} \frac{|y_j - Ag(\mathbf{A}^\dagger \mathbf{y}_i, \delta + \Delta)|_1}{|y_j|_1}}_{\text{Self-sup Loss}}. \end{aligned} \quad (10)$$

The first term, MR-INR Reconstruction Loss by measurement consistency, ensures that the MR-INR model reconstructs MRI images accurately. The second term, Self-Supervised Loss, refines the prediction using measurement consistency. This formulation enables adaptive single-slice refinement while preserving prior knowledge learned from the first stage.

### 4.3. Mathematical Analysis for Proposed Method

Here, we provide a view how the learned parameters  $\alpha$  and  $\beta$  enable effective adaptation under distribution shifts. Consider a test distribution:

$$Q: \mathbf{y} = \mathbf{x} + \mathbf{z}, \mathbf{x} = \mathbf{U}\mathbf{c} + \mu_Q, \mathbf{c} \sim \mathcal{N}(0, I), \mathbf{z} \sim \mathcal{N}(0, s^2 I). \quad (11)$$

Here,  $\mathbf{U} \in \mathbb{R}^{n \times d}$  is an orthonormal basis for the signal subspace, and  $\mu_Q$  represents the mean shift in the test distribution. Our goal is to estimate  $\mathbf{x}$  under this shift. The optimal test-time adaptation estimator is:

$$\hat{\mathbf{x}} = \alpha \mathbf{U}\mathbf{U}^T \mathbf{y} + \beta, \quad (12)$$

where  $\alpha$  adjusts for variance shifts, and  $\beta$  corrects mean shifts. The self-supervised loss is formulated as:

$$\begin{aligned} L_{SS}(\alpha, \beta) &= \mathbb{E}_Q [\|\mathbf{y} - \alpha \mathbf{U}\mathbf{U}^T \mathbf{y} - \beta\|_2^2] \\ &+ \frac{2\alpha d}{n-d} \mathbb{E}_Q [\|(\mathbf{I} - \mathbf{U}\mathbf{U}^T) \mathbf{y}\|_2^2]. \end{aligned} \quad (13)$$

Where the first term in loss function is for measurement consistency and the second term is for regularisation. Solving for the optimal  $\alpha^*$  and  $\beta^*$  by first-order derivatives (detailed proof in Supplementary), we obtain:

$$\alpha^* = \frac{1}{1 + s^2}, \quad \beta^* = \mu_Q. \quad (14) \quad (15)$$

Thus,  $\alpha$  and  $\beta$  optimise independently, where  $\alpha^*$  dynamically adapts to noise variance shifts, and  $\beta^*$  corrects mean shifts. Unlike prior TTT methods assuming zero-mean Gaussian distributions, our approach adapts to real-world MRI variations in less data with non-standard distribution. By integrating  $\alpha$  and  $\beta$  through MR-INR, our framework achieves robust adaptation under domain shifts, enhancing MRI reconstruction.

## 5. Experimental Settings

In this section, we describe the datasets, experimental configurations, domain shift scenarios, and comparative methods used to validate our proposed D2SA approach.

### 5.1. Datasets and Experimental Settings

We conduct experiments on multi-coil MRI datasets from **fastMRI** [36] (knee and brain) and **Stanford** [16]. Each experiment defines a source distribution  $\mathcal{S}$  and a target distribution  $\mathcal{T}$ , and we measure performance using SSIM, PSNR, and LPIPS. We evaluate two models: (1) **U-Net**: 8 layers, 64 channels, trained with Adam [20] at a learning rate of  $10^{-5}$ . (2) **VarNet**: 12 cascades, 18 channels, trained with Adam at a learning rate of  $10^{-4}$ . All other network training settings follow [11] and use a combination of supervised and self-supervised losses. We simulate  $4\times$  under-sampling by 1D cartesian mask with 8% auto-calibrating lines and estimating coil sensitivity maps via ESPIRiT [33]. We examine four domain-shift scenarios (*anatomy*, *dataset*, *modality*, and *acceleration*), evaluating both out-of-distribution ( $\mathcal{S} \rightarrow \mathcal{T}$ ) and in-distribution ( $\mathcal{T} \rightarrow \mathcal{T}$ ) performance (see these results in supplementary).

**Anatomy Shift.** We use U-Net and VarNet trained on fastMRI knee data ( $\mathcal{S}$ ) and fastMRI AXT2 brain data ( $\mathcal{T}$ ) following [11]. We additionally select 10 patients (110 AXT2 brain slices) subsampled at  $4\times$  for TTA evaluation.

**Dataset Shift.** We use U-Net and VarNet trained on Stanford knee data ( $\mathcal{S}$ ) and fastMRI knee data ( $\mathcal{T}$ ) from [11]. We further sample 20 patients (400 knee slices) from fastMRI under the same  $4\times$  subsampling for TTA evaluation.

**Modality Shift.** We adopt U-Net and VarNet trained on fastMRI AXT2 brain slices ( $\mathcal{S}$ ) and test on fastMRI AXT1PRE slices ( $\mathcal{T}$ ), as in [11]. We randomly select 10 patients (110 AXT1PRE brain slices) under  $4\times$  subsampling for TTA.

**Acceleration Shift.** Finally, we use U-Net and VarNet trained on knee measurements accelerated at  $2\times$  ( $\mathcal{S}$ ) [11], and evaluate on the same knee slices but accelerated at  $4\times$  ( $\mathcal{T}$ ). We select 20 patients (400 knee slices) for TTA.

Further details of training settings in stage 1 and 2 can be found in the supplementary.

### 5.2. Compared Methods

We compare D2SA with four related approaches:

- **DIP-TTT** [11]: A single-slice test-time training method based on Deep Image Prior (DIP).
- **FINE** [37]: A batch TTA technique using fidelity-based constraints.
- **Noiser2noise** [12, 24] and **SSDU** [35]: Self-supervised approaches suitable for patient-wise TTA.

DIP-TTT follows its original configuration, while FINE, Noiser2noise, and SSDU adopt the same training setup as

mentioned in the first stage of our proposed method. We further integrate our MR-INR component into these three methods to assess its efficacy in the patient-wise TTA. Finally, all pretrained patient-wise model with and without MR-INR by these frameworks are used for the second-stage single-slice refinement with setting mention in stage 2. Specifically, pretrained models without MR-INR only use self-supervised loss like DIP-TTT at the stage 2. All models are trained on a single RTX 3090 GPU.

## 6. Results

**Main results.** Tables 1 and 2 present the average performance (SSIM/PSNR/LPIPS) and test-time adaptation speed for U-Net and VarNet across four domain shifts: *Anatomy*, *Dataset*, *Modality*, and *Acceleration*.

Non-TTA perform the worst, as they lack generalisation to unseen distributions. DIP-TTT provides moderate improvements by leveraging SST, but it struggles with slow convergence and instability. Self-supervised methods (FINE, NR2N, SSDU) further improve reconstruction quality by introducing additional priors but still exhibit limitations in handling complex distribution shifts. Notably, these methods alone fail to match the performance of single-slice training, particularly in challenging domain shifts where mean and variance changes are significant.

Integrating MR-INR into self-supervised frameworks consistently enhances performance across all shifts. For example, in the anatomy shift scenario, NR2N+MR-INR in UNet improves SSIM from 0.836 (NR2N) to 0.949 and PSNR from 25.80 to 26.11, and FINE+MR-INR in VarNet improves SSIM from 0.696 (FINE) to 0.791 and PSNR from 21.39 to 25.30 in the acceleration shift. Even when the training time increases slightly compared with original FINE, NR2N, and SSDU, the performance of integrating MR-INR can reach or surpass the SSIM of DIP-TTT such as SSDU (UNet) in anatomy shift and NR2N (VarNet in dataset shift).

Furthermore, the patient-wise adaptation with MR-INR in the first stage enables a better initialisation, leading to more robust generalisation and improved efficiency in single-slice refinement. Although MR-INR introduces additional trainable parameters in the first stage, it significantly accelerates convergence in the second stage by providing a well-adapted initialisation. This results in more stable updates during single-slice refinement, ultimately achieving higher-quality reconstructions while reducing overall computational cost.

**Qualitative Results.** Figure 4 and 5 present visual comparisons of reconstructed images for the FINE-based UNet and VarNet methods in the anatomy shift and dataset shift respectively. More results of other distribution shifts are provided in the supplementary material.

Self-supervised methods without MR-INR (e.g., FINE)

Method (UNet)	Anatomy Shift ( $\mathcal{S}$ : Knee, $\mathcal{T}$ : Brain)	Dataset Shift ( $\mathcal{S}$ : Stanford, $\mathcal{T}$ : fastMRI)	Modality Shift ( $\mathcal{S}$ : AXT2, $\mathcal{T}$ : AXT1PRE)	Acceleration Shift ( $\mathcal{S}$ : 2x, $\mathcal{T}$ : 4x)
Zero-filling Non-TTA	0.737/24.50/0.327/- 0.625/21.77/0.458/-	0.754/24.33/0.359/- 0.559/21.87/0.454/-	0.747/25.7/0.350/- 0.794/27.18/0.391/-	0.754/23.371/0.396/- 0.726/23.37/0.396/-
DIP-TTT	0.859/27.05/0.322/42.1	0.810/28.08/0.298/40.8	0.846/27.61/0.361/31.5	0.815/27.93/0.299/95.3
FINE	0.834/25.98/0.351/4.9	0.796/26.54/0.319/6.4	0.825/26.71/0.377/5.6	0.782/25.75/0.333/6.6
FINE+MR-INR	0.845/26.37/0.346/5.5	0.807/26.84/0.314/6.6	0.835/26.51/0.373/6.0	0.793/26.29/0.326/7.0
FINE+SST	0.868/27.22/0.327/17.2	0.827/28.16/0.283/21.9	0.853/27.72/0.283/21.9	0.822/28.07/0.689/52.2
FINE+MR-INR+SST	0.876/27.71/0.320/12.1	0.829/28.34/0.279/18.7	0.861/27.93/0.279/15.7	0.825/28.54/0.286/31.9
NR2N	0.836/25.80/0.353/5.2	0.796/26.71/0.316/6.9	0.826/26.59/0.383/6.7	0.781/26.20/0.335/6.9
NR2N+MR-INR	0.849/26.11/0.346/5.7	0.798/26.42/0.317/7.4	0.829/26.64/0.380/7.3	0.791/26.37/0.332/7.5
NR2N+SST	0.868/27.38/0.323/21.7	0.825/28.23/0.284/22.5	0.854/27.69/0.284/22.6	0.822/28.07/0.291/52.7
NR2N+MR-INR+SST	0.871/27.32/0.323/12.2	0.830/28.43/0.279/16.4	0.862/27.98/0.279/14.5	0.825/28.86/0.287/31.7
SSDU	0.851/24.82/0.353/5.4	0.788/22.37/0.344/7.8	0.819/24.27/0.339/7.1	0.789/23.03/0.346/7.3
SSDU+MR-INR	0.861/25.18/0.348/5.6	0.789/22.45/0.339/8.0	0.832/24.97/0.385/7.4	0.797/23.78/0.344/7.7
SSDU+SST	0.871/25.17/0.349/25.3	0.825/28.35/0.284/30.6	0.854/27.71/0.287/25.7	0.823/28.07/0.293/139.8
SSDU+MR-INR+SST	0.877/27.46/0.322/11.5	0.828/28.36/0.287/18.9	0.860/28.04/0.287/17.4	0.826/28.62/0.286/44.2

Table 1. Performance comparison of UNet methods under different domain shifts. Each cell presents (**SSIM**  $\uparrow$  / **PSNR**  $\uparrow$  / **LPIPS**  $\downarrow$  / **Time (mins/patient)**  $\downarrow$ ). The family of proposed methods incorporates a self-supervised learning framework, combining MR-INR-based patient-wise adaptation with single-slice refinement using pre-trained patient-wise models.

Method (VarNet)	Anatomy Shift ( $\mathcal{S}$ : Knee, $\mathcal{T}$ : Brain)	Dataset Shift ( $\mathcal{S}$ : Stanford, $\mathcal{T}$ : fastMRI)	Modality Shift ( $\mathcal{S}$ : AXT2, $\mathcal{T}$ : AXT1PRE)	Acceleration Shift ( $\mathcal{S}$ : 2x, $\mathcal{T}$ : 4x)
Zero-filling Non-TTA	0.737/24.50/0.327/- 0.799/23.16/0.371/-	0.747/24.33/0.359/- 0.706/22.35/0.365/-	0.747/25.71/0.350/- 0.796/23.54/0.379/-	0.754/23.37/0.396/- 0.761/23.04/0.372/-
DIP-TTT	0.878/27.67/0.312/52.5	0.798/28.02/0.292/41.8	0.867/28.33/0.337/71.6	0.815/28.25/0.285/137.2
FINE	0.820/24.01/0.343/3.9	0.789/26.26/0.311/6.6	0.821/26.18/0.369/3.5	0.696/21.39/0.342/6.2
FINE+MR-INR	0.862/26.45/0.328/4.7	0.795/26.44/0.306/6.9	0.830/26.58/0.369/4.4	0.791/25.30/0.310/7.5
FINE+SST	0.862/27.57/0.311/53.5	0.794/27.72/0.294/20.3	0.857/28.08/0.345/79.8	0.823/28.17/0.288/63.8
FINE+MR-INR+SST	0.882/27.68/0.311/17.1	0.808/28.72/0.286/18.2	0.867/28.32/0.337/21.8	0.829/28.64/0.276/44.5
NR2N	0.827/23.95/0.334/4.9	0.798/26.59/0.299/6.8	0.827/25.60/0.368/4.1	0.718/20.97/0.327/6.6
NR2N+MR-INR	0.868/26.41/0.321/5.1	0.806/26.95/0.294/7.1	0.833/26.44/0.369/4.7	0.806/25.42/0.291/7.6
NR2N+SST	0.883/27.72/0.307/63.9	0.798/27.78/0.293/25.3	0.860/28.17/0.341/80.2	0.822/28.09/0.291/69.2
NR2N+MR-INR+SST	0.884/27.81/0.306/18.7	0.812/28.76/0.281/20.4	0.869/28.36/0.336/20.3	0.826/28.89/0.273/43.1
SSDU	0.738/20.87/0.375/5.1	0.737/20.43/0.349/7.2	0.746/22.59/0.391/4.4	0.556/16.93/0.421/7.4
SSDU+MR-INR	0.821/23.25/0.350/5.3	0.764/21.67/0.339/7.5	0.796/24.09/0.390/4.8	0.728/19.57/0.358/7.9
SSDU+SST	0.879/27.65/0.310/68.3	0.789/26.79/0.299/24.9	0.857/28.07/0.343/93.4	0.803/28.06/0.293/134.2
SSDU+MR-INR+SST	0.882/27.66/0.307/18.5	0.808/28.16/0.290/21.4	0.863/28.09/0.342/29.3	0.826/28.62/0.286/45.2

Table 2. Performance comparison of VarNet methods under different domain shifts. Each cell presents ((**SSIM**  $\uparrow$  / **PSNR**  $\uparrow$  / **LPIPS**  $\downarrow$  / **Time (mins/patient)**  $\downarrow$ ). The family of proposed methods incorporates a self-supervised learning framework, combining MR-INR-based patient-wise adaptation with single-slice refinement using pre-trained patient-wise models.

struggle to accurately adapt to domain variance, often producing hallucinations and artifacts, as highlighted in the error maps. While FINE+SST improves over FINE by incorporating single-slice adaptation, it lacks the AD module, leading to over-smoothing and loss of structural details. Our proposed approach, which integrates MR-INR with SST and AD, effectively balances adaptation and detail preservation, reducing hallucinations and enhancing reconstruction quality.

**Ablation Study.** Table 3 evaluates the impact of MR-INR and the AD module on UNet under anatomy shift (Knee to Brain). For patient-wise training, MR-INR improves adaptation, with a fixed latent code increasing PSNR and reducing parameter overhead. Allowing the latent code

to be learnable further enhances performance, demonstrating better patient-specific domain modelling. For single-slice training (SST), SST with learnable convolutional layers improves reconstruction. Combining it with MR-INR further boosts PSNR, confirming better initialisation from patient-wise adaptation. Adding the AD module slightly reduces PSNR but enhances structural preservation. Freezing convolutional layers (Frozen Convs + AD) achieves the best balance, preventing over-smoothing while maintaining efficiency.



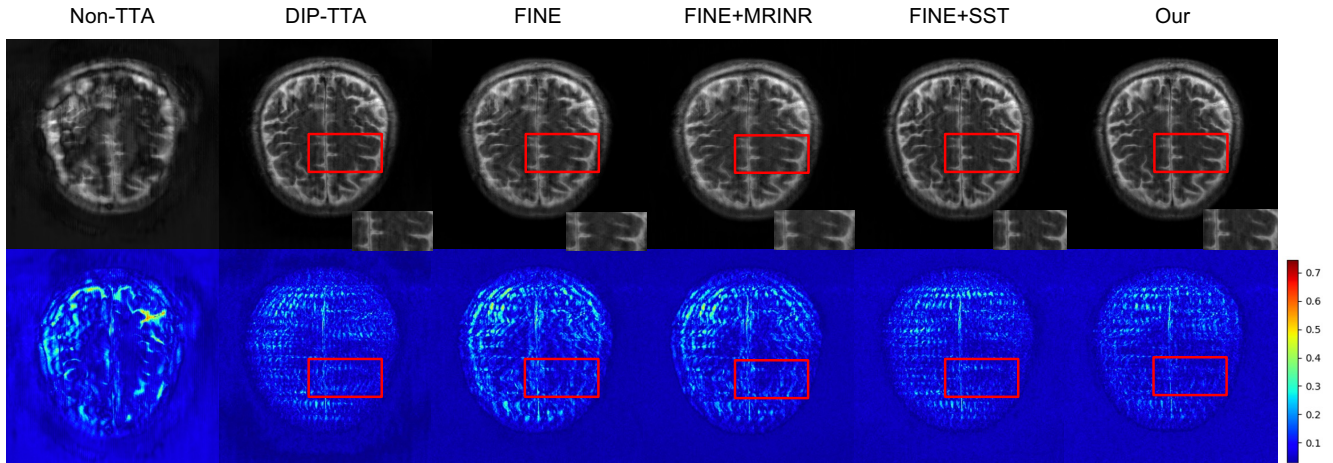


Figure 4. Comparison of different frameworks in UNet under anatomy shift (Knee to Brain) using the FINE method. The first row shows reconstructed MRI images, while the second row presents residual maps between reconstructions and full-sampled MRI. The proposed method (far right) achieves the lowest residuals, indicating improved reconstruction accuracy

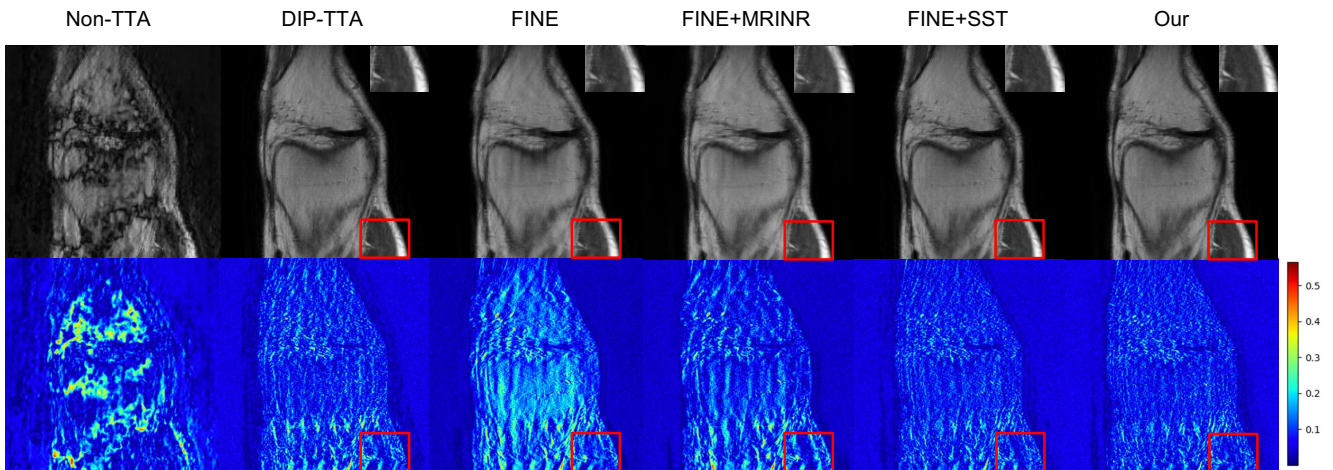


Figure 5. Comparison of different frameworks in VarNet under dataset shift (Stanford to fastMRI) using the FINE method. The first row shows reconstructed MRI images, while the second row presents residual maps between reconstructions and full-sampled MRI. The proposed method (far right) achieves the lowest residuals, indicating improved reconstruction accuracy

Stage	Method (UNet)	Knee $\rightarrow$ Brain
<b>Patient-wise training</b>	FINE	25.98/31.02/4.9
	+MR-INR + fixed latent code	26.37/31.29/5.3
	+MR-INR + learnable latent code	26.48/31.29/5.5
<b>Single-slice training (SST)</b>	+SST (learnable conv layers; no AD module)	27.22/31.02/17.2
	+MR-INR+SST (learnable conv layers; no AD module)	27.65/31.29/23.65
	+MR-INR+SST (learnable conv layers + AD module)	27.54/46.13/15.7
	+MR-INR+SST (Frozen conv layers + AD module)	27.71/17.89/12.1

Table 3. Ablation study on MR-INR and the AD module under anatomy shift (Knee to Brain) using UNet. Metrics are **PSNR/Number of Parameters (M, Millions) / Time per Patient (min)**. The first stage evaluates MR-INR with fixed and learnable latent codes (1408 parameters). The second stage compares SST configurations with MR-INR and AD.

## 7. Conclusion

We introduced Dual-Stage Distribution and Slice Adaptation (D2SA), a test-time adaptation framework that enhances MRI reconstruction under distribution shifts. By leveraging MR-INR, D2SA performs patient-wise adaptation to model mean/variance shifts and single-slice refinement using a learnable anisotropic diffusion (AD) module. This two-stage process improves generalisation, preserves structural details, and accelerates convergence. Experiments across four domain shifts (*Anatomy, Dataset, Modality, Acceleration*) show that D2SA consistently outperforms existing TTA methods, achieving higher SSIM/PSNR, lower LPIPS, and faster adaptation. Ablation studies confirm the effectiveness of MR-INR, AD modules, and frozen



convolutional layers in balancing efficiency and performance. While D2SA reduces adaptation time, further optimisation is still possible. Future work will explore integration with diffusion models for stronger priors and incremental learning to adapt continuously as new patients are introduced. Leveraging shared patient information could further improve generalisation, prevent forgetting, and accelerate convergence. So far, D2SA provides a robust, efficient solution for MRI reconstruction under test-time distribution shifts, with promising avenues for future refinement.

## 8. Acknowledgement

RS gratefully acknowledges the support from Future Network of Intelligence Institute, The Chinese University of Hong Kong (Shenzhen). ZD acknowledges the support from Wellcome Trust 221633/Z/20/Z and the funding from the Cambridge Centre for Data-Driven Discovery and Accelerate Program for Scientific Discovery, made possible by a donation from Schmidt Sciences. YC is funded by an AstraZeneca studentship and a Google studentship. CBS acknowledges support from the Philip Leverhulme Prize, the Royal Society Wolfson Fellowship, the EPSRC advanced career fellowship EP/V029428/1, EPSRC grants EP/S026045/1 and EP/T003553/1, EP/N014588/1, EP/T017961/1, the Wellcome Innovator Awards 215733/Z/19/Z and 221633/Z/20/Z, the European Union Horizon 2020 research and innovation programme under the Marie Skłodowska-Curie grant agreement No.777826 NoMADS, the Cantab Capital Institute for the Mathematics of Information and the Alan Turing Institute. AIAR gratefully acknowledges the support from Yau Mathematical Sciences Center, Tsinghua University.

## References

- [1] Rizwan Ahmad, Charles A Bouman, Gregory T Buzzard, Stanley Chan, Sizhuo Liu, Edward T Reehorst, and Philip Schniter. Plug-and-play methods for magnetic resonance imaging: Using denoisers for image recovery. *IEEE signal processing magazine*, 37(1):105–116, 2020.
- [2] Riccardo Barbano, Alexander Denker, Hyungjin Chung, Tae Hoon Roh, Simon Arridge, Peter Maass, Bangti Jin, and Jong Chul Ye. Steerable conditional diffusion for out-of-distribution adaptation in medical image reconstruction. *IEEE Transactions on Medical Imaging*, 2025.
- [3] Amir Beck and Marc Teboulle. A fast iterative shrinkage-thresholding algorithm for linear inverse problems. *SIAM journal on imaging sciences*, 2(1):183–202, 2009.
- [4] Kai Tobias Block, Martin Uecker, and Jens Frahm. Under-sampled radial mri with multiple coils. iterative image reconstruction using a total variation constraint. *Magnetic Resonance in Medicine: An Official Journal of the International Society for Magnetic Resonance in Medicine*, 57(6):1086–1098, 2007.
- [5] Emmanuel J Candès and Michael B Wakin. An introduction to compressive sampling. *IEEE signal processing magazine*, 25(2):21–30, 2008.
- [6] Tianxiang Chen, Zhentao Tan, Tao Gong, Qi Chu, Bin Liu, and Nenghai Yu. Feature preservation and shape cues assist infrared small target detection. *IEEE Transactions on Geoscience and Remote Sensing*, 2024.
- [7] Zixuan Chen, Zewei He, and Zhe-Ming Lu. Dea-net: Single image dehazing based on detail-enhanced convolution and content-guided attention. *IEEE Transactions on Image Processing*, 33:1002–1015, 2024.
- [8] Hyungjin Chung and Jong Chul Ye. Score-based diffusion models for accelerated mri. *Medical image analysis*, 80: 102479, 2022.
- [9] Hyungjin Chung and Jong Chul Ye. Deep diffusion image prior for efficient ood adaptation in 3d inverse problems. In *European Conference on Computer Vision*, pages 432–455. Springer, 2024.
- [10] Mohammad Zalbagi Darestani, Akshay S Chaudhari, and Reinhard Heckel. Measuring robustness in deep learning based compressive sensing. In *International Conference on Machine Learning*, pages 2433–2444. PMLR, 2021.
- [11] Mohammad Zalbagi Darestani, Jiayu Liu, and Reinhard Heckel. Test-time training can close the natural distribution shift performance gap in deep learning based compressed sensing. In *International Conference on Machine Learning*, pages 4754–4776. PMLR, 2022.
- [12] Arjun D Desai, Batu M Ozturkler, Christopher M Sandino, Robert Boutin, Marc Willis, Shreyas Vasanawala, Brian A Hargreaves, Christopher Ré, John M Pauly, and Akshay S Chaudhari. Noise2recon: Enabling snr-robust mri reconstruction with semi-supervised and self-supervised learning. *Magnetic Resonance in Medicine*, 90(5):2052–2070, 2023.
- [13] Emilien Dupont, Hyunjik Kim, SM Eslami, Danilo Rezende, and Dan Rosenbaum. From data to functa: Your data point is a function and you can treat it like one. *arXiv preprint arXiv:2201.12204*, 2022.

- [14] Emilien Dupont, Hyunjik Kim, S. M. Ali Eslami, Danilo Jimenez Rezende, and Dan Rosenbaum. From data to functa: Your data point is a function and you can treat it like one. In *39th International Conference on Machine Learning (ICML)*, 2022.
- [15] Amer Essakine, Yanqi Cheng, Chun-Wun Cheng, Lipei Zhang, Zhongying Deng, Lei Zhu, Carola-Bibiane Schönlieb, and Angelica I Aviles-Rivero. Where do we stand with implicit neural representations? a technical and performance survey. *Transactions on Machine Learning Research*, 2025. Survey Certification.
- [16] CUBE FSE'XL, PD PD, and FAT FAT. Creation of fully sampled mr data repository for compressed sensing of the knee. In *SMRT 22nd Annual Meeting, Salt Lake City, Utah, USA*. Citeseer, 2013.
- [17] Spyros Gidaris, Praveer Singh, and Nikos Komodakis. Un-supervised representation learning by predicting image rotations. *arXiv preprint arXiv:1803.07728*, 2018.
- [18] Kerstin Hammernik, Teresa Klatzer, Erich Kobler, Michael P Recht, Daniel K Sodickson, Thomas Pock, and Florian Knoll. Learning a variational network for reconstruction of accelerated mri data. *Magnetic resonance in medicine*, 79(6):3055–3071, 2018.
- [19] Kaiming He, Haoqi Fan, Yuxin Wu, Saining Xie, and Ross Girshick. Momentum contrast for unsupervised visual representation learning. In *Proceedings of the IEEE/CVF conference on computer vision and pattern recognition*, pages 9729–9738, 2020.
- [20] Diederik P Kingma and Jimmy Ba. Adam: A method for stochastic optimization. *arXiv preprint arXiv:1412.6980*, 2014.
- [21] Karl Krissian and Santiago Aja-Fernández. Noise-driven anisotropic diffusion filtering of mri. *IEEE transactions on image processing*, 18(10):2265–2274, 2009.
- [22] Jian Liang, Ran He, and Tieniu Tan. A comprehensive survey on test-time adaptation under distribution shifts. *International Journal of Computer Vision*, 133(1):31–64, 2025.
- [23] Michael Lustig, David Donoho, and John M Pauly. Sparse mri: The application of compressed sensing for rapid mr imaging. *Magnetic Resonance in Medicine: An Official Journal of the International Society for Magnetic Resonance in Medicine*, 58(6):1182–1195, 2007.
- [24] Nick Moran, Dan Schmidt, Yu Zhong, and Patrick Coady. Noisier2Noise: Learning to Denoise From Unpaired Noisy Data . In *2020 IEEE/CVF Conference on Computer Vision and Pattern Recognition (CVPR)*, pages 12061–12069, Los Alamitos, CA, USA, 2020. IEEE Computer Society.
- [25] Jeong Joon Park, Peter Florence, Julian Straub, Richard Newcombe, and Steven Lovegrove. Deepsdf: Learning continuous signed distance functions for shape representation. In *Proceedings of the IEEE/CVF conference on computer vision and pattern recognition*, pages 165–174, 2019.
- [26] Olaf Ronneberger, Philipp Fischer, and Thomas Brox. U-net: Convolutional networks for biomedical image segmentation. In *Medical image computing and computer-assisted intervention—MICCAI 2015: 18th international conference, Munich, Germany, October 5-9, 2015, proceedings, part III 18*, pages 234–241. Springer, 2015.
- [27] Jo Schlemper, Jose Caballero, Joseph V Hajnal, Anthony N Price, and Daniel Rueckert. A deep cascade of convolutional neural networks for dynamic mr image reconstruction. *IEEE transactions on Medical Imaging*, 37(2):491–503, 2017.
- [28] Zakhar Shumaylov, Jeremy Budd, Subhadip Mukherjee, and Carola Bibiane Schönlieb. Weakly convex regularisers for inverse problems: Convergence of critical points and primal-dual optimisation. In *Forty-first International Conference on Machine Learning*, page 6574, 2024.
- [29] Vincent Sitzmann, Julien Martel, Alexander Bergman, David Lindell, and Gordon Wetzstein. Implicit neural representations with periodic activation functions. *Advances in neural information processing systems*, 33:7462–7473, 2020.
- [30] Bowen Song, Liyue Shen, and Lei Xing. Piner: Prior-informed implicit neural representation learning for test-time adaptation in sparse-view ct reconstruction. In *Proceedings of the IEEE/CVF winter conference on applications of computer vision*, pages 1928–1938, 2023.
- [31] Anuroop Sriram, Jure Zbontar, Tullie Murrell, Aaron Defazio, C Lawrence Zitnick, Nafissa Yakubova, Florian Knoll, and Patricia Johnson. End-to-end variational networks for accelerated mri reconstruction. In *Medical image computing and computer assisted intervention—MICCAI 2020: 23rd international conference, Lima, Peru, October 4–8, 2020, proceedings, part II 23*, pages 64–73. Springer, 2020.
- [32] Matthew Tancik, Pratul Srinivasan, Ben Mildenhall, Sara Fridovich-Keil, Nithin Raghavan, Utkarsh Singhal, Ravi Ramamoorthi, Jonathan Barron, and Ren Ng. Fourier features let networks learn high frequency functions in low dimensional domains. *Advances in neural information processing systems*, 33:7537–7547, 2020.
- [33] Martin Uecker, Peng Lai, Mark J Murphy, Patrick Virtue, Michael Elad, John M Pauly, Shreyas S Vasanawala, and Michael Lustig. Espirit—an eigenvalue approach to autocalibrating parallel mri: where sense meets grappa. *Magnetic resonance in medicine*, 71(3):990–1001, 2014.
- [34] Zhiwen Wang, Zexin Lu, Tao Wang, Ziyuan Yang, Hui Yu, Zhongxian Wang, Yinyu Chen, Jingfeng Lu, and Yi Zhang. Test-time adaptation via orthogonal meta-learning for medical imaging. *IEEE Transactions on Radiation and Plasma Medical Sciences*, 2024.
- [35] Burhaneddin Yaman, Seyed Amir Hossein Hosseini, Steen Moeller, Jutta Ellermann, Kâmil Uğurbil, and Mehmet Akçakaya. Self-supervised learning of physics-guided reconstruction neural networks without fully sampled reference data. *Magnetic resonance in medicine*, 84(6):3172–3191, 2020.
- [36] Jure Zbontar, Florian Knoll, Anuroop Sriram, Tullie Murrell, Zhengnan Huang, Matthew J Muckley, Aaron Defazio, Ruben Stern, Patricia Johnson, Mary Bruno, et al. fastmri: An open dataset and benchmarks for accelerated mri. *arXiv preprint arXiv:1811.08839*, 2018.
- [37] Jinwei Zhang, Zhe Liu, Shun Zhang, Hang Zhang, Pascal Spincemille, Thanh D Nguyen, Mert R Sabuncu, and Yi Wang. Fidelity imposed network edit (fine) for solving ill-posed image reconstruction. *Neuroimage*, 211:116579, 2020.

- [38] Lipei Zhang, Yanqi Cheng, Lihao Liu, Carola-Bibiane Schönlieb, and Angelica I Aviles-Rivero. Biophysics informed pathological regularisation for brain tumour segmentation. In *International Conference on Medical Image Computing and Computer-Assisted Intervention*, pages 3–13. Springer, 2024.
- [39] Minghui Zhang, Hanxiao Zhang, Xin You, Guang-Zhong Yang, and Yun Gu. Implicit representation embraces challenging attributes of pulmonary airway tree structures. In *International Conference on Medical Image Computing and Computer-Assisted Intervention*, pages 546–556. Springer, 2024.
- [40] Yutian Zhao, Tianjing Zhang, and Hui Ji. Test-time model adaptation for image reconstruction using self-supervised adaptive layers. In *European Conference on Computer Vision*, pages 111–128. Springer, 2024.

# Supplementary Material

## 1. Training Details

**Stage 1: Functional-Level Patient Adaptation.** We train our INR-based model with a batch size of 2. One Adam learning rate of  $10^{-4}$  for weights in MR-INR and original network, and other one Adam learning rate of  $10^{-3}$  for learnable latent code. Epoch number sets to 25; training tends to stabilise after around 20 epochs. We initialise the 1D latent code (length  $1 \times 128$ ) with a zero-mean multivariate Gaussian ( $\sigma = 0.01$ ). For the SIREN [29] in our INR, we use a 4-layer network with 256 hidden units per layer, and default weight initialisation from [29]. The  $\lambda_{\text{self}}$ ,  $\lambda_{\text{INR}}$  and  $\lambda_{\text{reg}}$  in UNet are 1, 1 and  $1e^{-4}$  respectively. For VarNet, The  $\lambda_{\text{self}}$ ,  $\lambda_{\text{INR}}$  and  $\lambda_{\text{reg}}$  are set to 1,  $1e^{-3}$  and  $1e^{-4}$ .

**Stage 2: Single-Slice Refinement.** We then refine each slice using a learnable Anisotropic Diffusion module, freezing the original convolutional layers. The learning rate is  $10^{-4}$  with Adam, and we run up to 1000 steps. Following [11], we perform self-validation by reserving 5% of the signals; if the validation error increases, we terminate TTA early. The  $\lambda_{\text{self}}$ ,  $\lambda_{\text{INR}}$  in UNet are 1 and 1. respectively. For VarNet, The  $\lambda_{\text{self}}$  and  $\lambda_{\text{INR}}$  are set to 1 and  $1e^{-3}$ .

All MR signals are under-sampled in acceleration rate  $\times 2$  or  $\times 4$  by 1D cartesian mask with 8% auto-calibrating lines. More details can be found in provided demo code.

## 2. Other Quantitative Results in Same Domain Shift

In this section of the supplementary material, we provide additional metric evaluation results to further analyse the impact of in-domain shifts. These evaluations offer a more comprehensive comparison of model performance under varying conditions.

Tables 4 and 5 compare the performance (SSIM/PSNR/LPIPS) and test-time adaptation speed of U-Net and VarNet across four same-domain shifts.

**Computational Efficiency and Convergence.** Although MR-INR increases training time in the first stage, it significantly accelerates convergence, particularly in brain-to-brain adaptation. In contrast, DIP-TTT suffers from slow convergence due to the absence of a well-initialisation on patient-wise representation, leading to unstable updates during single-slice adaptation.

**Impact of Acceleration Masks.** Even at the same acceleration rate, variations in sampling masks introduce inconsistencies that impact reconstruction performance in the second single-slice training. Non-TTT methods struggle to generalise other unseen data in same dataset and acceleration rate effectively, whereas MR-INR can mitigate performance degradation by modelling patient-specific mean and variance shifts. This highlights the importance of functional-level adaptation in stabilising test-time learning under in-domain shifts.

**Conclusion.** Overall, AnySSL+MR-INR+SST achieves the best balance between adaptation quality, structural preservation, and computational efficiency. The integration of MR-INR enables faster convergence and greater robustness to in-domain distribution shifts, demonstrating its effectiveness in improving MRI reconstruction.



Method (UNet)	Anatomy ( $T$ : Brain)	Dataset ( $T$ : fastMRI)	Modality ( $T$ : AXT1PRE)	Acceleration ( $T$ : 2x)
sero-filling Non-TTT	0.737/24.50/0.359/- 0.822/26.50/0.358/-	0.754/24.33/0.359/- 0.559/21.88/0.454/-	0.747/25.70/0.350/- 0.799/26.08/0.395/-	0.846/26.52/0.226/- 0.149/15.74/0.580/-
DIP-TTT	0.876/27.45/0.323/46.1	0.806/28.43/0.281/62.9	0.858/27.87/0.354/15.1	0.834/28.63/0.207/95.4
FINE	0.847/26.39/0.345/4.6	0.799/26.88/0.309/6.9	0.837/26.88/0.368/4.5	0.846/26.07/0.275/7.1
FINE+MR-INR	0.852/26.66/0.343/13.5	0.805/27.08/0.312/7.2	0.839/27.28/0.366/4.7	0.878/28.40/0.229/7.4
FINE+SST	0.874/27.36/0.327/17.0	0.824/28.14/0.285/33.2	0.860/27.82/0.285/11.3	0.893/30.02/0.675/59.1
FINE+MR-INR+SST	0.878/27.59/0.320/13.5	0.825/28.44/0.287/29.1	0.862/28.06/0.280/9.3	0.901/30.15/0.195/39.3
NR2N	0.850/26.11/0.347/4.8	0.799/26.92/0.307/7.3	0.835/26.88/0.374/4.7	0.836/25.09/0.286/7.2
NR2N+MR-INR	0.857/26.18/0.345/5.0	0.803/26.99/0.298/7.6	0.836/26.95/0.378/5.1	0.870/25.56/0.242/7.6
NR2N+SST	0.875/27.49/0.323/20.7	0.825/28.20/0.283/33.5	0.865/27.88/0.283/12.6	0.892/30.03/0.207/60.0
NR2N+MR-INR+SST	0.876/27.46/0.322/13.1	0.826/28.35/0.281/30.4	0.866/28.16/0.281/11.2	0.900/30.07/0.196/39.3
SSDU	0.861/25.16/0.347/5.0	0.794/22.64/0.332/7.5	0.848/25.40/0.375/5.2	0.804/20.73/0.311/7.4
SSDU+MR-INR	0.865/25.36/0.323/5.3	0.8018/22.71/0.335/7.7	0.826/24.06/0.335/5.6	0.833/21.41/0.279/7.7
SSDU+SST	0.876/27.39/0.323/24.1	0.823/28.13/0.291/42.7	0.860/27.58/0.291/13.4	0.741/24.71/0.280/90.2
SSDU+MR-INR+SST	0.879/27.57/0.322/11.5	0.825/28.17/0.285/35.4	0.863/28.14/0.285/11.2	0.838/29.20/0.218/49.7

Table 4. Performance comparison of UNet methods under the same domain shifts. Each cell presents ((**SSIM**  $\uparrow$  / **PSNR**  $\uparrow$  / **LPIPS**  $\downarrow$  / **Time (mins/patient)**  $\downarrow$ ). The family of proposed methods incorporates a self-supervised learning framework, combining MR-INR-based patient-wise adaptation with single-slice refinement using pre-trained patient-wise models.

Method (VarNet)	Anatomy ( $T$ : Brain)	Dataset ( $T$ : fastMRI)	Modality ( $T$ : AXT1PRE)	Acceleration ( $T$ : 2x)
sero-filling Non-TTT	0.754/24.33/0.359/- 0.845/24.60/0.305/-	0.747/24.33/0.359/- 0.706/23.12/0.331/-	0.747/25.7/0.350/- 0.838/22.48/0.354/-	0.846/26.52/0.226/- 0.149/15.74/0.580/-
DIP-TTT	0.875/27.29/0.315/102.4	0.815/28.28/0.282/57.1	0.869/28.33/0.331/25.8	0.840/29.26/0.196/120.4
FINE	0.854/26.49/0.328/3.9	0.801/26.55/0.300/7.2	0.862/27.70/0.335/3.5	0.816/24.17/0.273/7.4
FINE+MR-INR	0.857/26.66/0.325/4.7	0.804/26.80/0.297/7.8	0.855/27.46/0.343/4.2	0.857/26.62/0.225/7.8
FINE+SST	0.877/27.62/0.310/91.9	0.809/27.87/0.289/30.4	0.873/28.41/0.329/26.2	0.832/29.07/0.204/63.8
FINE+MR-INR+SST	0.884/27.81/0.306/47.6	0.825/28.34/0.278/23.5	0.862/28.16/0.337/19.1	0.860/29.30/0.198/44.3
NR2N	0.868/26.82/0.321/4.4	0.815/26.95/0.285/7.8	0.871/27.43/0.332/4.3	0.805/23.37/0.285/7.6
NR2N+MR-INR	0.868/26.97/0.319/5.1	0.808/26.48/0.290/8.1	0.859/27.14/0.340/4.9	0.835/25.71/0.248/8.0
NR2N+SST	0.880/27.69/0.307/110.3	0.812/27.77/0.288/33.7	0.878/28.53/0.323/26.8	0.838/29.05/0.199/59.3
NR2N+MR-INR+SST	0.885/27.81/0.306/49.7	0.826/28.42/0.279/22.9	0.867/28.27/0.331/18.4	0.844/29.24/0.191/45.7
SSDU	0.838/24.69/0.344/4.7	0.686/19.12/0.370/8.2	0.825/22.81/0.376/4.8	0.597/17.44/0.366/8.1
SSDU+MR-INR	0.839/24.89/0.342/5.1	0.713/19.72/0.350/8.7	0.809/22.18/0.369/5.3	0.695/19.02/0.318/8.5
SSDU+SST	0.881/27.57/0.310/127.2	0.802/27.77/0.289/40.7	0.871/28.31/0.331/30.4	0.819/26.07/0.243/70.5
SSDU+MR-INR+SST	0.887/27.57/0.310/50.4	0.815/28.29/0.285/39.2	0.867/28.20/0.333/24.7	0.826/28.62/0.286/50.1

Table 5. Performance comparison of VarNet methods under the same domain shifts. Each cell presents ((**SSIM**  $\uparrow$  / **PSNR**  $\uparrow$  / **LPIPS**  $\downarrow$  / **Time (mins/patient)**  $\downarrow$ ). The family of proposed methods incorporates a self-supervised learning framework, combining MR-INR-based patient-wise adaptation with single-slice refinement using pre-trained patient-wise models.

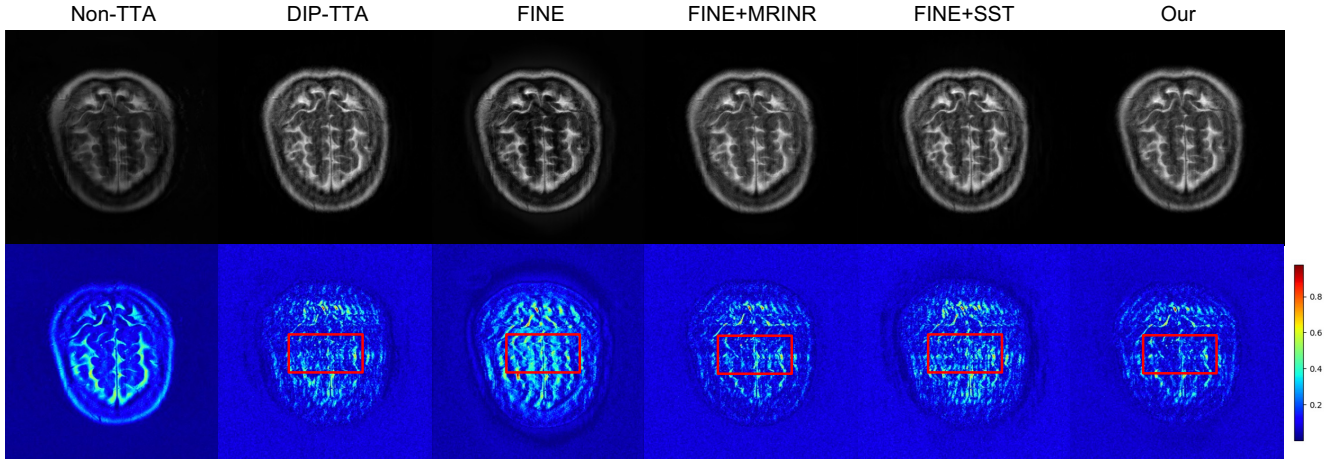


Figure 6. Comparison of different frameworks in VarNet under anatomy shift (Knee to Brain) using the FINE method. The first row shows reconstructed MRI images, while the second row presents residual maps between reconstructions and full-sampled MRI.

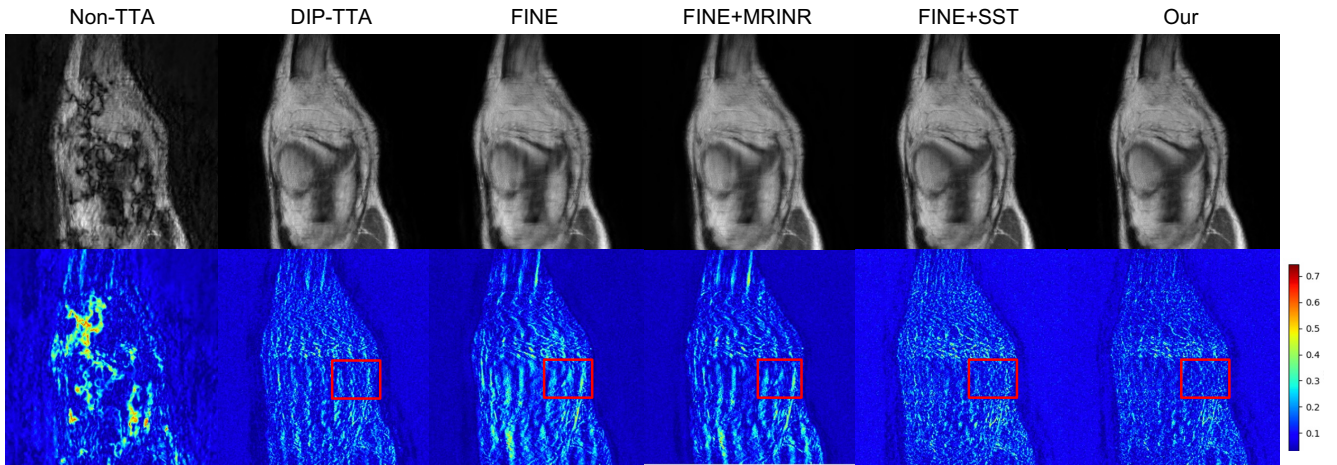


Figure 7. Comparison of different frameworks in Unet under dataset shift (Stanford to fastMRI) using the FINE method. The first row shows reconstructed MRI images, while the second row presents residual maps between reconstructions and full-sampled MRI.

### 3. Other Visualisations

Additionally, we present extended the rest of visualisation results illustrating the domain shift effects on Unet and VarNet, highlighting differences in reconstruction quality and generalisation behaviour across shifts. In Figures 6,7,8,9,10, and 11, the first row displays the reconstructed MRI images, while the second row shows the residual maps (differences between the reconstructed and fully-sampled MRI images).

For all domain shifts, our method consistently demonstrates significantly reduced noise and better pattern distribution, with fewer artifacts and hallucinations. The residual maps further highlight this, as our method shows much lower residuals, indicating more accurate reconstructions. This improvement is particularly evident across all shifts: anatomy (Figures 6), dataset (Figures 7), modality (Figures 8 and 9), and acceleration (Figures 10 and 11). These results underscore the effectiveness of our proposed method in handling domain shifts, with notable improvements in generalisation and reconstruction quality, particularly with respect to artifacts reduction and structural detail preservation.



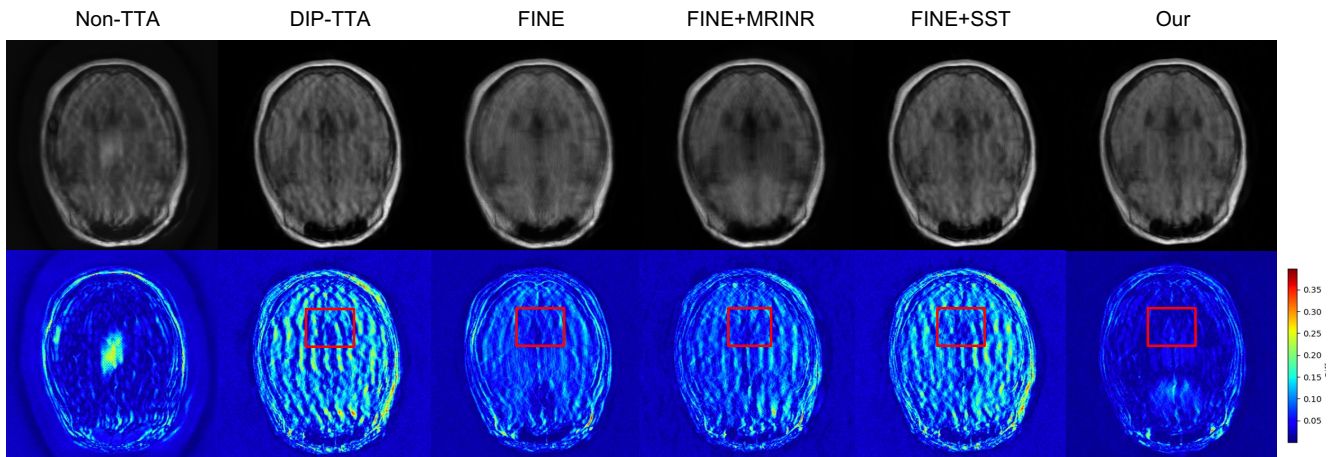


Figure 8. Comparison of different frameworks in Unet under modality shift (AXT2 to AXT1PRE) using the FINE method. The first row shows reconstructed MRI images, while the second row presents residual maps between reconstructions and full-sampled MRI.

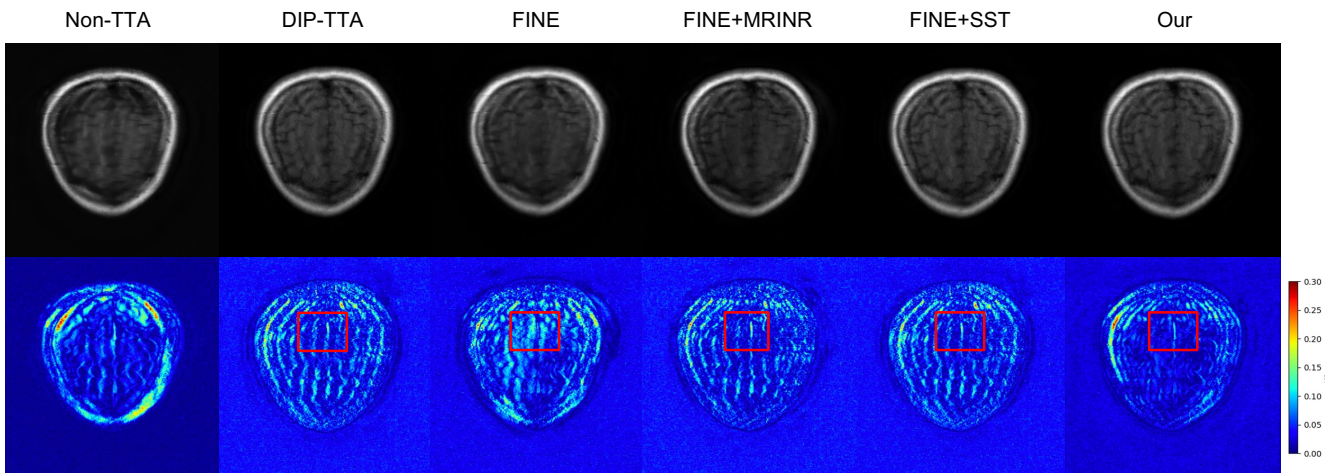


Figure 9. Comparison of different frameworks in Varnet under modality shift (AXT2 to AXT1PRE) using the FINE method. The first row shows reconstructed MRI images, while the second row presents residual maps between reconstructions and full-sampled MRI.

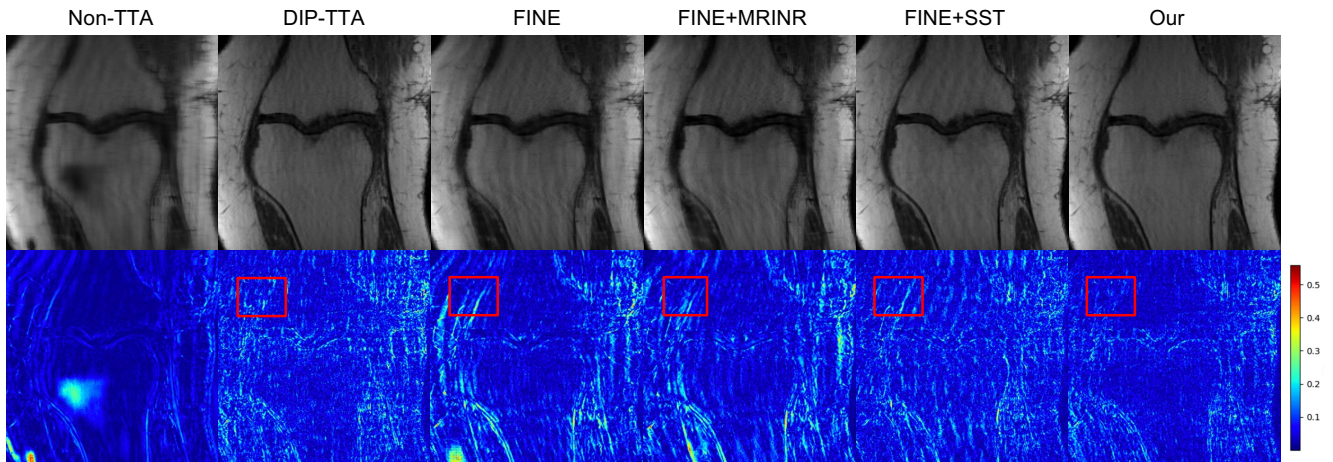


Figure 10. Comparison of different frameworks in Unet under acceleration shift (2X to 4X) using the FINE method. The first row shows reconstructed MRI images, while the second row presents residual maps between reconstructions and full-sampled MRI.

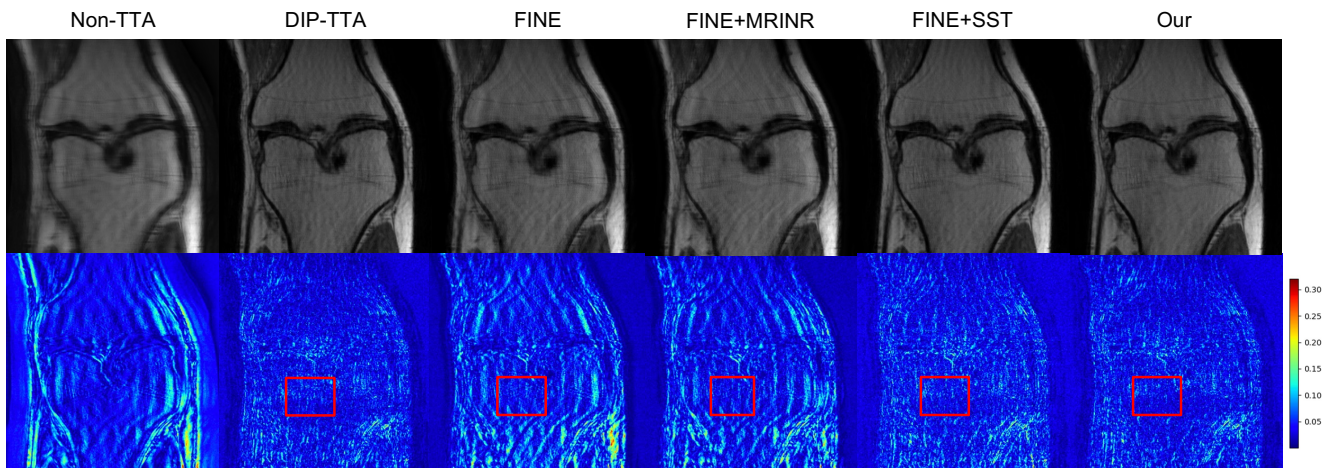


Figure 11. Comparison of different frameworks in Varnet under acceleration shift (2X to 4X) using the FINE method. The first row shows reconstructed MRI images, while the second row presents residual maps between reconstructions and full-sampled MRI.



## 4. Mathematical Analysis for Proposed Method

### 4.1. Test Distribution and Problem Formulation

We consider a setting where the observed signal  $\mathbf{y}$  is a corrupted version of the underlying clean signal  $\mathbf{x}$ , which follows the test distribution:

$$Q : \mathbf{y} = \mathbf{x} + \mathbf{z}, \quad \mathbf{x} = \mathbf{U}\mathbf{c} + \mu_Q, \quad \mathbf{c} \sim \mathcal{N}(0, I), \quad \mathbf{z} \sim \mathcal{N}(0, Is^2). \quad (16)$$

Here,  $\mathbf{U} \in \mathbb{R}^{n \times d}$  is an orthonormal basis for the signal subspace, and  $\mu_Q$  represents the mean shift in the test distribution. Our goal is to estimate  $\mathbf{x}$  under this distribution shift.

### 4.2. Self-Supervised Adaptation for Domain Shift

To address the distribution shift from  $P$  to  $Q$ , we introduce an adaptation mechanism that accounts for both variance and mean shifts. The optimal estimator for  $\mathbf{x}$  under test-time training (TTT) is:

$$\hat{\mathbf{x}} = \alpha \mathbf{U}\mathbf{U}^T \mathbf{y} + \beta, \quad (17)$$

where  $\alpha$  accounts for variance shifts, and  $\beta$  corrects for mean shifts.

The self-supervised loss function is defined as:

$$L_{SS}(\alpha, \beta, \mathbf{U}, \mathbf{y}) = \mathbb{E}_Q [\|\mathbf{y} - \alpha \mathbf{U}\mathbf{U}^T \mathbf{y} - \beta\|_2^2] + \frac{2\alpha d}{n-d} \mathbb{E}_Q [\|(\mathbf{I} - \mathbf{U}\mathbf{U}^T)\mathbf{y}\|_2^2]. \quad (18)$$

**Expanding the First Term of  $L_{SS}$ :**

$$\begin{aligned} \mathbb{E}_Q [\|\mathbf{y} - \alpha \mathbf{U}\mathbf{U}^T \mathbf{y} - \beta\|_2^2] &= \mathbb{E}_Q [\mathbf{y}^T \mathbf{y} - 2\alpha \mathbf{y}^T \mathbf{U}\mathbf{U}^T \mathbf{y} - 2\beta^T \mathbf{y} \\ &\quad + \alpha^2 \mathbf{y}^T \mathbf{U}\mathbf{U}^T \mathbf{U}\mathbf{U}^T \mathbf{y} + 2\alpha \beta^T \mathbf{U}\mathbf{U}^T \mathbf{y} + \beta^T \beta]. \end{aligned} \quad (19)$$

Taking expectation:

$$\begin{aligned} \mathbb{E}_Q [\mathbf{y}^T \mathbf{y}] - 2\alpha \mathbb{E}_Q [\mathbf{y}^T \mathbf{U}\mathbf{U}^T \mathbf{y}] - 2\mathbb{E}_Q [\beta^T \mathbf{y}] \\ + \alpha^2 \mathbb{E}_Q [\mathbf{y}^T \mathbf{U}\mathbf{U}^T \mathbf{U}\mathbf{U}^T \mathbf{y}] + 2\alpha \mathbb{E}_Q [\beta^T \mathbf{U}\mathbf{U}^T \mathbf{y}] + \mathbb{E}_Q [\beta^T \beta]. \end{aligned} \quad (20)$$

Compute Individual Expectations and using expectation properties:

$$\mathbb{E}_Q [\mathbf{y}^T \mathbf{y}] = \text{tr}(\mathbb{E}_Q [\mathbf{y}\mathbf{y}^T]). \quad (21)$$

Since:

$$\mathbb{E}_Q [\mathbf{y}\mathbf{y}^T] = \mathbf{U}\mathbf{U}^T + s^2 I + \mu_Q \mu_Q^T, \quad (22)$$

$$\mathbb{E}_Q [\mathbf{y}^T \mathbf{y}] = \text{tr}(\mathbf{U}\mathbf{U}^T) + s^2 \text{tr}(I) + \text{tr}(\mu_Q \mu_Q^T), \quad (23)$$

$$= d + s^2 n + \|\mu_Q\|^2. \quad (24)$$

For the second expectation:

$$\mathbb{E}_Q [\mathbf{y}^T \mathbf{U}\mathbf{U}^T \mathbf{y}] = \text{tr}(\mathbf{U}\mathbf{U}^T \mathbb{E}_Q [\mathbf{y}\mathbf{y}^T]). \quad (25)$$

Substituting  $\mathbb{E}_Q [\mathbf{y}\mathbf{y}^T]$ :

$$\mathbb{E}_Q [\mathbf{y}^T \mathbf{U}\mathbf{U}^T \mathbf{y}] = \text{tr}(\mathbf{U}\mathbf{U}^T (\mathbf{U}\mathbf{U}^T + s^2 I + \mu_Q \mu_Q^T)), \quad (26)$$

$$= \text{tr}(\mathbf{U}\mathbf{U}^T) + s^2 \text{tr}(\mathbf{U}\mathbf{U}^T) + \text{tr}(\mathbf{U}\mathbf{U}^T \mu_Q \mu_Q^T), \quad (27)$$

$$= d + s^2 d + \text{tr}(\mathbf{U}\mathbf{U}^T \mu_Q \mu_Q^T). \quad (28)$$

$$L_{SS}(\alpha, \beta) = (d + s^2n + \|\mu_Q\|^2) - 2\alpha(d + s^2d + \text{tr}(\mathbf{U}\mathbf{U}^T \mu_Q \mu_Q^T)) - 2\beta^T \mu_Q + \alpha^2 d + 2\alpha d \beta^T \mu_Q + \|\beta\|^2. \quad (29)$$

Combine each component, we can get

$$L_{SS}(\alpha, \beta) = d + s^2n + \|\mu_Q\|^2 - 2\alpha(d + s^2d + \|\mathbf{U}^T \mu_Q\|^2) + \alpha^2 d + 2\alpha d \beta^T \mu_Q - 2\beta^T \mu_Q + \|\beta\|^2 \quad (30)$$

Final Simplified Expression for this term

$$L_{SS}(\alpha, \beta) = s^2n + (1 - \alpha)^2 d + (\alpha^2 - 2\alpha)s^2d + \|\beta - \mu_Q\|^2 \quad (31)$$

**Expanding second term:**

$$\frac{2\alpha d}{n-d} \mathbb{E}_Q [\|(\mathbf{I} - \mathbf{U}\mathbf{U}^T)\mathbf{y}\|_2^2]. \quad (32)$$

First, expanding the squared norm:

$$\|(\mathbf{I} - \mathbf{U}\mathbf{U}^T)\mathbf{y}\|_2^2 = ((\mathbf{I} - \mathbf{U}\mathbf{U}^T)\mathbf{y})^T ((\mathbf{I} - \mathbf{U}\mathbf{U}^T)\mathbf{y}). \quad (33)$$

Since  $(\mathbf{I} - \mathbf{U}\mathbf{U}^T)$  is symmetric:

$$= \mathbf{y}^T (\mathbf{I} - \mathbf{U}\mathbf{U}^T) \mathbf{y}. \quad (34)$$

Taking expectation:

$$\mathbb{E}_Q [\mathbf{y}^T (\mathbf{I} - \mathbf{U}\mathbf{U}^T) \mathbf{y}] = \text{tr} ((\mathbf{I} - \mathbf{U}\mathbf{U}^T) \mathbb{E}_Q [\mathbf{y}\mathbf{y}^T]). \quad (35)$$

Using the expectation property:

$$\mathbb{E}_Q [\mathbf{y}\mathbf{y}^T] = \mathbf{U}\mathbf{U}^T + s^2 I + \mu_Q \mu_Q^T. \quad (36)$$

Substituting:

$$= \text{tr} ((\mathbf{I} - \mathbf{U}\mathbf{U}^T) (\mathbf{U}\mathbf{U}^T + s^2 I + \mu_Q \mu_Q^T)). \quad (37)$$

Expanding the trace:

$$= \text{tr} ((\mathbf{I} - \mathbf{U}\mathbf{U}^T) s^2 I + (\mathbf{I} - \mathbf{U}\mathbf{U}^T) \mu_Q \mu_Q^T). \quad (38)$$

Since  $(\mathbf{I} - \mathbf{U}\mathbf{U}^T)$  removes the  $\mathbf{U}\mathbf{U}^T$  component:

$$= s^2(n-d) + \text{tr} ((\mathbf{I} - \mathbf{U}\mathbf{U}^T) \mu_Q \mu_Q^T). \quad (39)$$

Thus, the second term simplifies to:

$$\frac{2\alpha d}{n-d} [s^2(n-d) + \text{tr} ((\mathbf{I} - \mathbf{U}\mathbf{U}^T) \mu_Q \mu_Q^T)]. \quad (40)$$

Assuming  $\mu_Q$  is entirely inside the subspace spanned by  $\mathbf{U}$ , the projection term vanishes, giving:

$$\frac{2\alpha d}{n-d} s^2(n-d). \quad (41)$$

Last, we take final simplification Now, simplifying the terms:

$$L_{SS}(\alpha, \beta) = s^2n + (1 - \alpha)^2 d + (\alpha^2 - 2\alpha)s^2d + \|\beta - \mu_Q\|^2 + 2\alpha d s^2. \quad (42)$$

Combining the  $s^2d$  terms:

$$(\alpha^2 - 2\alpha)s^2d + 2\alpha s^2d = \alpha^2s^2d - 2\alpha s^2d + 2\alpha s^2d = \alpha^2s^2d. \quad (43)$$

Thus, the final loss function simplifies to:

$$L_{SS}(\alpha, \beta) = s^2n + (1 - \alpha)^2d + \alpha^2s^2d + \|\beta - \mu_Q\|^2. \quad (44)$$

**Finally, we compute the derivatives**

For derivative with Respect to  $\alpha$

$$\frac{\partial L_{SS}}{\partial \alpha} = -2d(1 - \alpha) + 2\alpha ds^2 + \frac{2d}{n - d}(s^2n - s^2d). \quad (45)$$

Setting this to zero and solving for  $\alpha^*$ :

$$\alpha^* = \frac{1}{1 + s^2}. \quad (46)$$

For derivative with Respect to  $\beta$

$$\frac{\partial L_{SS}}{\partial \beta} = 2(\beta - \mu_Q). \quad (47)$$

Setting this to zero and solving for  $\beta^*$ :

$$\beta^* = \mu_Q. \quad (48)$$

In conclusion,

1.  $\alpha^*$  dynamically adjusts for noise variance shifts.
2.  $\beta^*$  corrects for mean shifts, making adaptation robust in OOD settings.